Computational Fluid Dynamics Study of a Cross-Flow Marine Hydrokinetic Turbine and the Combined Influence of Struts and Helical Blades

Preprint

Will Wiley,[1] Thanh Toan Tran,[1] Michael Lawson,[1] and Matthew Barrington[2]

1 National Renewable Energy Laboratory
2 Ocean Renewable Power Company

Presented at the ASME 2023 42nd International Conference on Ocean, Offshore and Arctic Engineering (OMAE 2023)
Melbourne, Australia
June 11–16, 2023

Contract No. DE-AC36-08GO28308

Computational Fluid Dynamics Study of a Cross-Flow Marine Hydrokinetic Turbine and the Combined Influence of Struts and Helical Blades

Preprint

Will Wiley,[1] Thanh Toan Tran,[1] Michael Lawson,[1] and Matthew Barrington[2]

1 National Renewable Energy Laboratory
2 Ocean Renewable Power Company

NOTICE

COMPUTATIONAL FLUID DYNAMICS STUDY OF A CROSS-FLOW MARINE HYDROKINETIC TURBINE AND THE COMBINED INFLUENCE OF STRUTS AND HELICAL BLADES

Will Wiley[1], Thanh Toan Tran[1], Michael Lawson[1], Matthew Barrington[2]

[1]National Renewable Energy Laboratory, Golden, CO
[2]Ocean Renewable Power Company, Portland, ME

ABSTRACT

A computational fluid dynamics study was performed for a cross-flow marine hydrokinetic turbine. The analysis was done in three dimensions and used the unsteady Reynolds-averaged Navier-Stokes solver in the commercial code STAR-CCM+. The base turbine configuration is the RivGen® Turbine, designed by the Ocean Renewable Power Company. A convergence and uncertainty analysis was performed for both the spatial and temporal discretization; this was done using the base configuration, which features support struts and helical foils. Both struts and helical blades introduce three-dimensional flow effects, influencing the complex flow phenomenon of dynamic stall. The study compares the relative impact of struts on power performance and blade loading for both helical and straight blades, and found that for this turbine the relative loss in power from struts was lower with helical blades.

Keywords: cfd, cross-flow turbine, mhk turbine, dynamic stall

1. INTRODUCTION

A diverse portfolio of renewable energy types will be needed to most effectively transition to clean energy. This includes the growing field of marine energy. Marine energy devices include marine hydrokinetic (MHK) turbines, wave energy converters, and ocean thermal energy converters. MHK turbines can be powered by river, tidal, or ocean currents. Each of these technologies has unique applications for which they can provide the most benefit.

MHK river turbines are well suited to provide electrical power to coastal communities, and the robust, independent technology can be particularly attractive for remote locations without a larger grid connection. River current is relatively consistent and predictable, and population centers are often located close to strong resources. A 2012 report from the Electric Power Research Institute found that the continental United States has a theoretical river power resource of 1381 TWh/yr and a technically recoverable resource of 119.9 TWh/yr [1]. The theoretical resource includes only river segments with a mean flow rate greater than 1000 cfs, and the technical resource then limits the locations by water depth and flow velocity, and limits the power by turbine spacing and efficiency [1].

Similar to a wind turbine, an MHK turbine can have a rotation axis that is either parallel to the freestream flow direction (axial flow turbine) or perpendicular to the freestream flow direction (cross-flow turbine). In the wind industry, axial flow turbines have become the standard; they have more constant loading and power production throughout a rotor revolution. In contrast, cross-flow turbines inherently have a continually changing flow and loading. The highly dynamic forces can lead to fatigue problems, but cross-flow turbines offer some advantages. There is more flexibility in the location of the main bearing, and the blades can potentially be supported at both ends. This can allow for easier access for maintenance and shorter support towers, particularly for wind turbines. Cross-flow turbines typically have a rectangular projected area that can be well suited for optimized layouts in a tidal channel or river. The axis of rotation is perpendicular to the flow direction, so assuming that the flow direction is always in a two-dimensional plane, typically parallel to the ground, no yaw motion is needed. This is particularly helpful for tidal currents, which change direction multiple times per day.

Cross-flow turbines can have blades that are driven either by drag (Savonius) or driven by lift (Darrieus); lift-dominated turbines can achieve much higher efficiencies and are the focus of most utility-scale design. Lift force on a foil is perpendicular to the relative inflow velocity (W) and has some component that creates positive rotor torque. The relative velocity for a foil section changes in both direction and magnitude throughout a rotation. These changes are dependent on the ratio of the relative flow due to rotation (u_{tip}), and the freestream velocity (u_∞), known as the tip speed ratio (TSR), as defined in Equation 1:

$$TSR = \frac{u_{tip}}{u_\infty} = \frac{\omega R}{u_\infty} \tag{1}$$

1

Figure 1 shows the relative angle of inflow compared to the chord line, known as the angle of attack or α, and the magnitude of the relative inflow velocity compared to the freestream velocity, both as a function of azimuth angle, θ. The azimuth angle describes where a blade section is within a rotation as described by the coordinate system in Figure 2. At $\theta = 90°$ and $\theta = -90°$, the foil motion is directly into and out of the inflow, respectively. At these points, $\alpha = 0°$. On the upstream side of the rotation ($90° < \theta < 270°$), α is negative and first increases in magnitude slowly, before decreasing in magnitude quickly. On the downstream side of the rotation ($-90° < \theta < 90°$), α is positive and first increases in magnitude quickly, before decreasing in magnitude slowly. When the rotation speed is constant, changes with respect to θ are proportional to changes with respect to time, and $\frac{\partial \alpha}{\partial t}$ has important effects on dynamic stall.
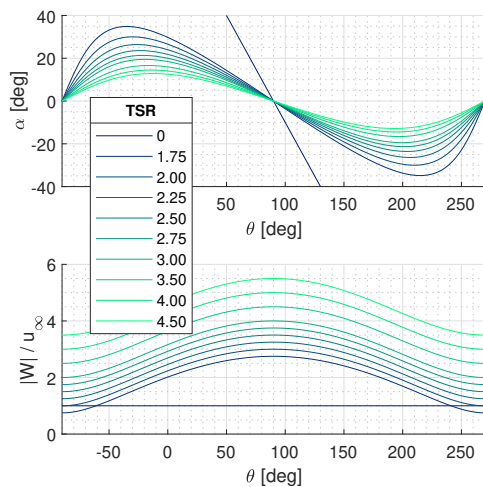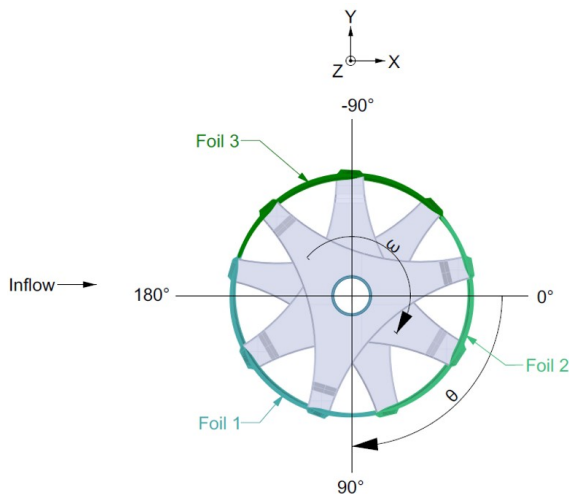

FIGURE 1: CROSS-FLOW TURBINE INFLOW VELOCITY

FIGURE 2: COORDINATE SYSTEM

At $\alpha = 0°$ there is no lift; in theory, as α increases from here, the lift force also increases, until a certain angle where stall occurs. Stall is when the the flow can no longer remain attached

to the suction side of the foil, detaching, causing a rapid decrease in velocity on this side of the foil and an increase in pressure, which results in a rapid decrease in lift force. For a given foil in a steady flow of a certain velocity, this phenomenon will occur at a consistent value of α. However, when the angle of attack is changing dynamically, the boundary layer can possibly stay attached longer, changing the stall phenomenon. This is known as dynamic stall, and it is a critical flow effect for cross-flow turbines. Typically, dynamic effects cause stall to occur at a larger value of α, but with a more sudden drop in lift force [2].

The changing angle of attack and inflow velocity leads to periodically changing loading on the blades. This results in an unsteady torque on the rotor with peaks from each of the blades. The unsteady loading can be difficult for the generator and for structural fatigue. Some turbine designers have developed helical blades, where the azimuth angle varies along the span. This results in each section of the blade experiencing minimum and maximum loads at different times, smoothing out the net loading for the rotor.

There are some negative to using helical blades. One key drawback is the construction cost due to higher complexity in manufacturing. Hydrodynamically, a helical blade introduces some flow in the spanwise direction, which can reduce lift and subsequently the power output.

The impact of different helix angles has been previously studied. March et al. and Divakaran et al. both performed computational fluid dynamics (CFD) analyses of three-bladed cross-flow turbines with different helix angles [3] [4]. Both groups tested a range of angles up to $120°$, where the tip of one blade is at the same azimuth angle as the opposite tip of another blade. In each study it was found that power production diminishes as the helix angle becomes large, but the variation in the rotor loads throughout the rotation was reduced with increasing angle [3] [4]. It should be noted that both studies featured a turbine with a relatively small span-to-diameter ratio, increasing the hydrodynamic influence of a given helix angle. Both analyses also concluded that the TSR with the highest coefficient of power generally increased with helix angle [3] [4].

Cross-flow turbine blades need to be connected to the rotor shaft in some way. Various methods have been used, including an eggbeater-type shape, where the tips of the blades bend inward to meet the shaft. Typically for marine turbines, some form of a strut is used to transfer the forces from the blades to the shaft. While necessary, these struts always introduce some drag and lead to some decrease in power generation. The University of Washington performed an extensive experimental study in a recirculating water flume to assess the impacts of different strut shapes and positions [5]. They tested ten different configurations, including three strut cross-sectional shapes, two strut thicknesses, and two different spanwise strut locations; they also considered three different setups with solid disks. The work concluded that strut thickness and shape both had significant impacts on the net power production; thinner and more streamlined struts performed best. Struts placed at the tips of the blades also significantly outperformed mid-span struts; the flow constraint at the tips reduced tip losses, actually increasing power [5]. The friction drag of the disk supports was found to be too large to benefit from the

reduced form drag, and the group's work concluded that for a three-bladed turbine, struts are a better choice [5].

The previously mentioned CFD projects that studied the effect of helix angle both used an unsteady Reynolds-averaged Navier-Stokes (URANS) code with a k–ω shear stress transport (SST) turbulence model [3] [4]. This is a commonly used and validated modeling approach in the marine industry. Dynamic stall, however, is a complex phenomenon, which is inherently unsteady and largely influenced by turbulence and boundary layer effects, making it difficult to accurately predict. Rezaeiha et al. compared three numerical methods for modeling the dynamic stall of a cross-flow turbine: URANS, scale-adaptive simulation (SAS), and hybrid RANS/large eddy simulation (stress-blended eddy simulation or SBES), in order of increasing fidelity [2]. The URANS model in the Rezaeiha project used a four-equation transition model; compared to the previously mentioned two-equation k–ω SST, this model does not assume turbulent flow everywhere but tries to predict the point of transition and the following influence of turbulence on the mean flow. The analysis was done only in two dimensions, making the higher-fidelity modeling more computationally feasible. The size and position of formation and detachment of both the dynamic stall vortex and the trailing-edge vortex were compared to evaluate the performance of the models. These vortices drive the unique lift progression of dynamic stall and are critical to predicting the power generation and fatigue loading of a cross-flow turbine. The three models agree reasonably well until the point where the dynamic stall vortex detaches from the leading edge. The two lower-fidelity models predict earlier detachment and then an earlier drop in lift and rotor torque. The middle-fidelity SAS model does a better job of matching the SBES model with respect to the strength of this vortex. The URANS model, however, does a better job of matching the SBES model with respect to the time of detachment for the trailing-edge vortex [2].

The work of Rezaeiha et al. points to the significant difficulty in modeling dynamic stall, even in the much less computationally expensive two-dimensional domain. The comparisons were also only presented for the upstream half of the rotor's revolution. This portion of the motion has a slower rate of change in angle of attack than the other half of the revolution, making it easier to model. In addition to a more quickly changing angle of attack, the downstream stroke also passes through the wake of the upstream stroke (and shaft, if included), adding further complexity and uncertainty.

2. OBJECTIVE

The current work evaluates the loads on a cross-flow MHK turbine to better understand the power generation and fatigue loading on the structure. The subject turbine is the RivGen® Power System, designed by the Ocean Renewable Power Company (ORPC). Figure 3 shows an image from ORPC of the device sitting above the water. The turbine has two rotors, each with three helical blades, connected to the drive shaft with three struts.

The loading of a turbine like this is inherently unsteady and is driven by the complex phenomenon of dynamic stall. Even high-fidelity models in two-dimensional domains do not agree on the exact timing and influence of the stall patterns. It is

FIGURE 3: ORPC RIVGEN POWER SYSTEM [6]

acknowledged that there will be some uncertainty in the prediction of the phenomenon with any CFD modeling, and the goal is to better understand and quantify that uncertainty and evaluate the ability of numerical tools in this problem.

Three-dimensional effects from helical blades and struts have been found to significantly impact the net power and load cycle of similar turbines. Previous works looked at the impacts of these two turbine features separately. It is predicted that the spanwise influence of the helix angle and the struts interact with each other, changing the hydrodynamic impact of both. This project aims to describe the combined coupled influence by comparing the relative losses from struts with both helical and straight-bladed turbines.

3. BACKGROUND

3.1 ORPC RivGen Turbine

The ORPC RivGen Power System is a tested technology; it was deployed in the Kvichak River in Igiugig, Alaska, operating as the longest running marine energy project in the Americas [6]. The device is designed to have minimal impact on the marine environment, and this was verified at the Igiugig site [6]. ORPC states that the turbine can be rated for up to 80 kW and can operate in a maximum current speed of 3.5 m/s [6].

As shown in Figure 3, the turbine generator unit has pontoons on each end, which sit on the river floor, and a faired platform beneath the rotors. The support structure is symmetric and holds identical rotors on each half. Each rotor is made of three helical foils and three faired struts. The struts are arranged with one at the center of the foil span and the other two partway between the foil tips and the middle strut.

3.2 Computational Methods

The commercial CFD code STAR-CCM+ was used for the analysis. This tool has been widely used and validated in the marine modeling space. The free surface was modeled using the volume of fluid method with a water and an air phase. This is important to capture any free surface impacts from the turbine. Differences in hydrostatic pressure on the blades can have important impacts on the blade loading of an MHK turbine. The URANS formulation was used with a second-order implicit time model and second-order upwind convection for velocity and turbulence. The high-resolution interface-capturing scheme was used for the volume fraction convection.

3

The URANS method is based on the time-averaged values of velocity and pressure and treats turbulent fluctuations as a change to viscosity known as the turbulent viscosity. In this work, the model used for determining this influence of turbulence on the mean flow is the $k-\omega$ SST model. Two variables, k, the turbulent kinetic energy, and ω, the specific turbulent dissipation rate—are used to calculate vt, the turbulent viscosity. The SST model blends the solution of the standard $k-\omega$ model near walls with the related standard $k-\epsilon$ model far from walls. This blending method reduces the dependence of the solution on the freestream value of the specific dissipation rate (a common problem in the standard $k-\omega$ model) [7].

The fluid domain was composed of two regions, a stationary background region and a rotating turbine region. A sliding interface was used between the two regions. The cylindrical interface was fixed in size and space, so there was no overlap between the regions, and all cells were used in every time step. The sliding interface in STAR-CCM+ does not need cell boundaries to match exactly at the interface (conformal mesh); the solver is able to interpolate for neighboring cell values. Smooth flow continuity between regions does require that the cell sizes and aspect ratios on each side of the interface are roughly equal.

The background region uses a hexahedral mesh in line with the main free-flow direction. This mesh type can efficiently capture free surfaces by using fine resolution in the vertical direction, where sharp changes in volume of fluid, velocity, and pressure may exist, and by using coarser resolution in the two horizontal direction where gradients are expected to be smaller.

The rotating turbine region uses a polyhedral mesh. This mesh type is better for capturing complex curved geometry, such as the foils and the struts. Polyhedral cells typically have a low aspect ratio and are not aligned with any particular direction. This is advantageous for the rotating region, as the flow direction through the cells will be continuously changing.

Prism layer cells or extruded cells are used on all nonslip surfaces in the domain. This includes all the rotor components, the support structure, and the river floor. These high aspect ratio cells take advantage of the known discrepancy in gradients in the directions away from and across walls. The cells are very small in the direction normal to the wall to capture the sharp changes in the boundary layer but are the same size as the outer mesh in the other two dimensions, reducing computational cost. Capturing the highly dynamic loads on the foils requires very fine resolution in the boundary layer. On the foils, the first cell thickness is kept within the linear viscous sublayer, corresponding to y^+ values close to 1.0, and no higher than 5.0. All y^+ treatment is used for the less sensitive non-foil surfaces.

3.3 Computational Domain

The computational fluid domain size is shown in Figure 4. The symmetry of the turbine was leveraged for computational efficiency by using a symmetry plane to cut the domain in half. Only one rotor and one pontoon were modeled, and a symmetric boundary condition was used on the dividing surface. The domain extended 12.75 m away from this plane in the z-direction. The water depth is 5.1 m, and 3.0 m of air was included above the still free surface. A distance of 20.0 m was included upstream

of the turbine, and 30.0 m downstream. The inlet of the domain used a velocity inlet boundary condition with a uniform current velocity profile with a speed of 1.75 m/s in the x-direction. A pressure outlet boundary condition was used on the opposite end of the domain. A symmetry plane, which acts as a slip wall, was used on the side of the domain opposite the turbine center. The river floor was modeled as a no-slip wall, creating some boundary layer profile in the velocity. The top of the domain was modeled as a velocity inlet.
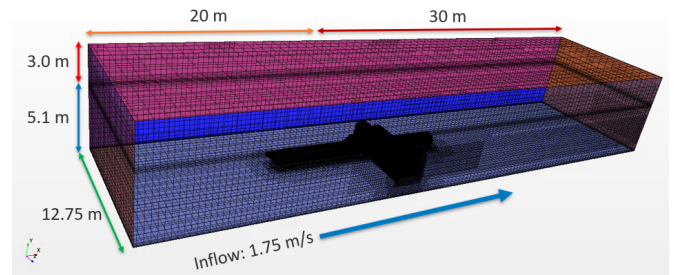

FIGURE 4: COMPUTATIONAL DOMAIN SIZE

3.4 Recorded Data

Discretized load knowledge is helpful for structural design and provides understanding of the three-dimensional hydrodynamics. The forces and moments were recorded on small foil segments, split in the spanwise direction (z). The breakup is shown in Figure 5; each foil has a total of 50 segments. Note that segments 1 and 50 refer to the foil tips, and segments 9–10, 25–26, and 41–42 refer to the segments where the struts attach to the blades. The loads on the three struts, shaft, and support structure were also separately tracked.
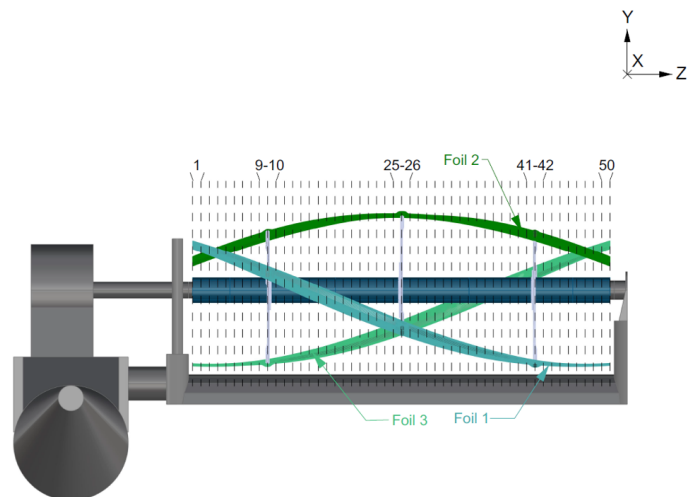

FIGURE 5: TURBINE SPANWISE SEGMENT DIAGRAM

The foil loads were post-processed into lift and drag terms to observe the occurrence of dynamic stall. For these calculations, the inflow velocity and angle relative to the foil section is based on the undisturbed current. This assumption will not always be true due to wake effects and flow augmentation from the support. A velocity probe could be used upstream of the foil section for an

4

instantaneous local inflow, however there is no clear location for this probe, and there is no way to dissect the foil's influence on the flow from the observed field. The vorticity in some characteristic cross sections was also recorded to visualize the production and shedding of the leading edge and trailing-edge vortices.

Simulations were run, and the net power and system drag were monitored for each revolution. The models were run until these two parameters had converged to stabilized values.

4. CONVERGENCE STUDY

The progression of the recorded loads and the visualization of the vorticity was tracked while varying the discretization of the simulation in order to make sure that the results were independent of the modeling choices. This convergence study was performed with the base RivGen Turbine design featuring helical blades and support struts. The convergence study focused on two TSRs: one close to the expected peak power performance and one at the bottom of the tested TSR range, where the largest changes in angle of attack are seen. The larger changes in angle of attack are likely to have more pronounced dynamic stall effects, making this a potentially more sensitive condition.

4.1 Mesh

The influence of a few mesh parameters was studied in the spatial discretization convergence study. Some refinements were kept constant through all the iterations.

The region around the expected free surface featured a refinement zone with cells 3 times shorter in the vertical direction as the base water mesh. Close to the turbine, where more free-surface deformation is expected, this refinement zone extended slightly further from the mean water line. There were two wake refinement zones: a coarser zone with a cell length half the size of the base water mesh, and a finer zone with a cell length a quarter the size of the base water mesh. The finer wake zone extends two diameters downstream of the rotor, and the coarser wake zone extends to the outlet of the domain. The mesh on the surface of the support structure had a reduced cell length 8 times smaller than the base water mesh, and the cell growth rate extending out from the surface was reduced to create a refined region to capture the flow around the support. The final refinement in the background region was around the sliding interface, set to match the cell size of the rotating region, 16 times smaller than the base water mesh. The total thickness of all prism layer cells in the background region was held fixed and tried to match the expected boundary layer thickness approximated by a flat plate.

In the turbine region, the first cell thickness on the foils was held constant to maintain the same low y^+ value below 5.0. When the size of the outer polyhedral cells was iterated, the prism layer cell total thickness and number of cells were adjusted to maintain a smooth transition from the prism layers to the polyhedral cells. The cells on the surface of the foil were set to be 128 times smaller than the base water mesh, which correlates to roughly 130 cells around the perimeter of the foil section, depending on the base size. Various cell types and refinement levels were tested at the trailing edge. A coarser surface refinement was used on the shaft and the struts.

The first mesh convergence check was a traditional scaling of the base mesh size, with refinement zones that follow accordingly. This study is helpful for confidence in the large-scale flow over the turbine and support structure. Four different resolutions were tested. In addition to these base meshes, two more were tested with variations to the mesh along the foils' trailing edges.

The first trailing-edge mesh used the same prism layer properties as were used on the rest of the foil surface. This results in prism layer cells that wrap around the trailing edge, as shown in Figure 6a. Prism layer cells typically wrap all the way around a body, but in this case the cells along the trailing edge do not work well. Prism layer cells have a high aspect ratio, which is useful along a wall where you expect high gradients along the cell's short dimension and small gradients along the cell's long dimension. It can be assumed that the flow will separate exactly at the trailing edge corner on the pressure side of the foil. This results in a sharp free-shear layer, with large gradients along the wrapped cell's long dimension. One possible solution is to extrude prism layers along a virtual plane extending out of the trailing edge, resulting in cells that can capture the high gradient in the free-shear layer. Unfortunately, the continually varying angle of attack, with changes up to 70°, makes this approach unusable for a cross-flow turbine. Instead, low-aspect-ratio cells are needed to capture the constantly changing trailing-edge flow. Figure 6b shows an example where the prism layers are truncated approaching the trailing edge and transition into refined polyhedral cells.
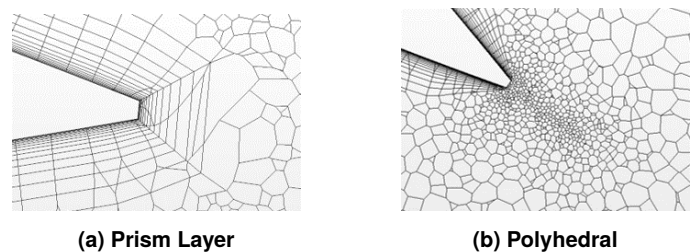

(a) Prism Layer   **(b) Polyhedral**

FIGURE 6: TRAILING-EDGE MESH TYPES

The resolution in this region needs to be high for a smooth transition from the prism layer cells and to capture the important trailing edge dynamics. Rezaeiha et al. found that differences in the formation and shedding of the trailing-edge vortex between their three numerical models led to significant changes in rotor torque, demonstrating the importance of predicting flow in this region well [2].

Table 1 gives the cell count for the four base refinement levels and the two variations using polyhedral cells at the trailing edge. These two meshes both use the same settings as the third mesh in all other areas of the domain. They differ in the size of the polyhedral cells along the line extending out of the trailing edge. Changing only the mesh along the trailing edge, which is roughly 200 times shorter than the foil chord length, results in total domain cell counts 21% and 77% larger, demonstrating the computational efficiency of prism layers.

Figure 7 shows some summary values from the base cell size study. These include the total drag on the turbine, including the support structure, the power coefficient, and the standard deviation of the torque throughout one rotation. The plotted

5

TABLE 1: BASE MESH REFINEMENT STUDY

Trailing Edge Cell Type	Base Cell Length [m]	Cell Count [Millions]		
		Background	Turbine	Total
Prism Layer	0.6	1.08	10.30	11.38
	0.5	1.67	12.51	14.18
	0.4	2.39	15.24	17.64
	0.3	4.07	32.75	36.82
Poly-hedral	0.4	2.39	28.89	31.29
	0.4	2.39	18.99	21.38

values are all normalized relative to the maxima. The left and right side of the figure show the same information, but with different limits on the y-axis, to visualize both the local trends and the global variation.
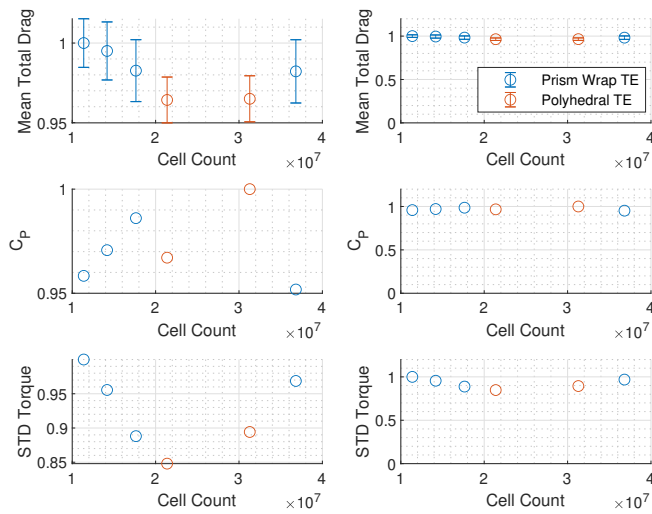

FIGURE 7: MESH CONVERGENCE VALUES RELATIVE TO MAXIMUM; LEFT Y-AXIS FOR LOCAL TRENDS AND RIGHT Y-AXIS FOR GLOBAL VARIATION

Inspection of the velocity and vorticity fields at the trailing edge shows a much more physical flow pattern when using polyhedral cells. A section of the velocity field is shown in Figure 8. When comparing the summary results in Figure 7, there does not appear to be a clear distinction between the mesh styles. However, when comparing the load progression through a rotation and along the span, the differences are more distinct. On the upstream stroke, the mesh with the polyhedral cells has consistently larger stall angles, and the torque recovers more quickly down helix from the strut.

For all meshes, the loads on the upstream stroke are much more consistent. In this half of the rotation, the inflow is much cleaner, and the rate of change in angle of attack is also slower. Both result in more stable loads from rotation to rotation. A significant portion of the variability in the summary values comes from the uncertain fluctuating nature of the downstream stroke.

Figure 9 displays the influence of the disturbed inflow on the downstream stroke. Figure 9a shows the vorticity field in a
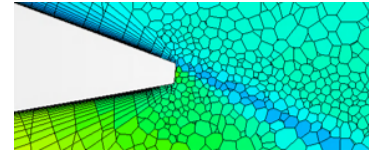

FIGURE 8: VELOCITY FIELD BEHIND TRAILING EDGE WITH POLYHEDRAL CELLS

2D simulation with a very high mesh resolution (0.04 m base cell length). The wake effects of the foils and the shaft are very pronounced in 2D. Figure 9b shows a time history of the moment on each foil over two rotations. The peaks in the moment occur on the upstream stroke and are very consistent; on the downstream stroke, there is significant variation. Because the shaft shedding frequency is different from the foil passing frequency, each foil stroke interacts in a different way. The time history of the vorticity field was used to record the interaction of each foil's downstream stroke, with the main shaft wake vortex, and it is marked in the figure. A back miss indicates a near miss close to the trailing edge, and a front miss indicates a near miss close to the leading edge. The load progression on the blade is clearly strongly linked to the wake interaction, which varies for every rotation.
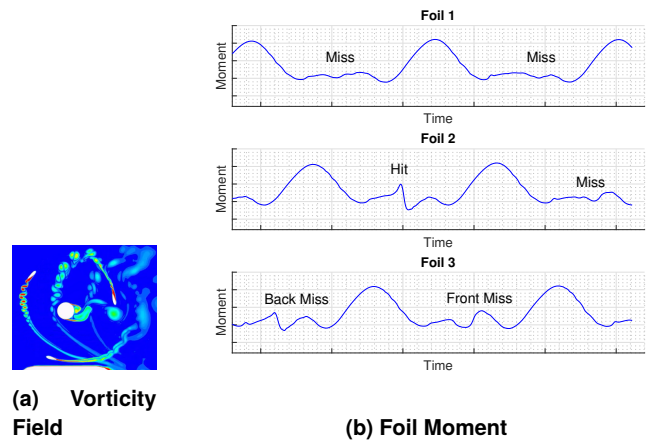

(a) Vorticity Field

(b) Foil Moment

FIGURE 9: 2D EFFECT OF SHAFT WAKE VORTEX COLLISION

It should be noted that while still important, this effect is much weaker in 3D. The correlation length for the wake structures is shorter than the blade span, and turbulent mixing in the spanwise direction further weakens the vortex structures. The sharp effect on the foil is further dampened by the helix in the blades. Instead of clean discretely different downstream events, the 3D downstream stroke has a rough uncertain load pattern.

In a balance of computation cost and flow prediction accuracy, the base mesh with polyhedral trailing-edge cells, and a total of 21.38 million cells, was selected.

4.2 Time

A time step study was performed using the selected base mesh. Four different time steps were tested, and the resulting loads were compared using the lowest tested TSR of 1.75. It

This report is available at no cost from the National Renewable Energy Laboratory at www.nrel.gov/publications.

was predicted that the time step would be most dependent on the Courant number in the near-foil region. In this moving area, the velocity of the fluid relative to the wall mesh will always be zero at the wall, so the Courant number will not necessarily increase with TSR. Instead, it was predicted that the lowest TSR may be the most sensitive to the time step, given the largest changes in angle of attack, inducing the most dynamic flow structures.

The resulting loads are shown in the top half of Figure 10. The moments displayed are the summation of the torque on each entire foil. The legend shows how many time steps are used per revolution. As previously discussed, the downstream stroke, where negative moments appear at this TSR, is highly variable due to wake effects. Convergence will be evaluated based on the upstream stroke. All time steps result in a double humped peak in torque for each foil, with some dip in the middle. The dip occurs because of the middle strut and its impact on the foil sections adjacent to it; the load at a given spanwise section only has a single peak. The size of the dip appears to be the most sensitive result to the time step. The bottom half of Figure 10 shows the convergence of the minimum torque in the dip as a function of time steps per revolution.
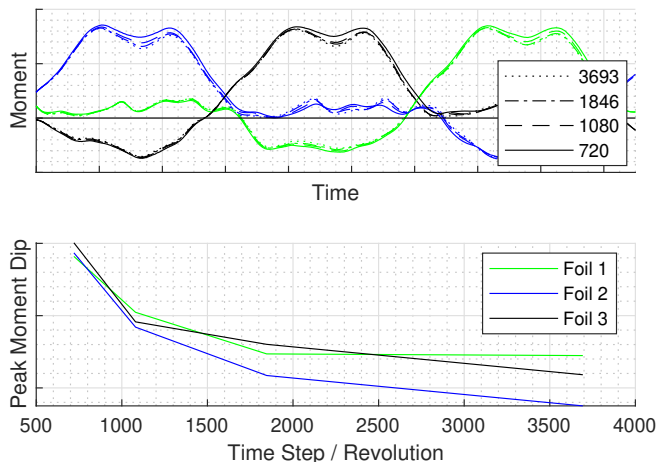

FIGURE 10: TIME STEP CONVERGENCE

Based on the results of this study, the second largest time step was selected, which correlates to 1080 time steps per revolution. This factor of 1080 is used for all TSRs, so that the time step decreases with increased rotor speed, further limiting the possible Courant numbers.

4.3 Boundary Layer Mesh

Given the known challenges with predicting dynamic stall, special attention was given to the boundary layer modeling on the foils. A 2D study was performed to efficiently assess the sensitivity of a number of parameters, including using the k–ϵ turbulence model, a larger y^+ value with wall functions, extremely fine mesh in the full turbine region, and different expansion ratios in the prism layers. It was found that the prism layer expansion ratio was the parameter with the most sensitivity.

The expansion ratio is the thickness factor between one prism layer cell and the following prism layer cell away from the wall.

A constant factor was used in this work. The base convergence study used a factor of 1.3, which is near the upper limit of best practice for important unsteady boundary layers, although the default setting suggested by STAR-CCM+ is 1.5 [7]. Lower ratios of 1.2, 1.15, and 1.1 were tested in a 3D study as well. Changing the expansion ratio does not lead to a typical monotonic convergence experienced with a standard spatial discretization convergence study. The refinement here drives the development and trajectory of the vortices, which create the load patterns on the foil. A lower expansion ratio is also not inherently better. In all iterations, the first cell thickness on the wall was kept constant to maintain the same low y^+ value. If there is a large jump in cell size from the outermost prism layer cell to the outer volume mesh, the interface will act as a numerical boundary altering the flow at this point. The outer mesh was originally kept the same as from the base mesh convergence study. To achieve a smooth transition then, a lower expansion ratio requires a larger total thickness of the prism layers. The cell count of these meshes is shown in the upper part of Table 2, in the "Base" row.

As the expansion ratio gets low, the required thickness grows exponentially. Prism layers are effective because the flow near the wall has sharp gradients in a known direction, but further from the wall, the direction of the largest gradients can no longer be assumed. It does not make sense to use prism layers here. A second iteration of reduced expansion ratio limited the total thickness. In this mesh, for a smooth transition to the outer polyhedral mesh, the outer cell size needs to be reduced to match the outermost prism layer. The total cell count for this mesh is shown in the bottom part of Table 2, in the "Matched" row.

TABLE 2: EXPANSION RATIO

Polyhedral Outer Mesh	Expansion Ratio	Total Cell Count [millions]
Base	1.30	21.4
	1.20	25.5
	1.15	30.3
	1.10	33.8
Matched	1.15	168.9

Note that there is a huge increase in total cell count with a matched outer mesh, almost 6 times larger than the corresponding base mesh. A cell count of 168.9 million is a prohibitively large number for a full test matrix, but it was run at a single TSR to assess the sensitivity.

Figure 11 shows the torque on foil section 17 of foil 1, as described in Figure 5, for one period. This foil section is relatively far from any strut or blade tip and provides a somewhat representative view of the main power-producing segments of the turbine. The lines plotted with only a number use the base outer mesh, and the number indicates the expansion ratio. The lines plotted with a "p" before the number for the expansion ratio use a matched polyhedral outer mesh with a limited total prism layer thickness.

The lines plotted with a "t" after the mesh description use a different number of time steps per turbine revolution. It was expected that the required time step is likely a function of the near-foil cell size, so a combined study was performed.
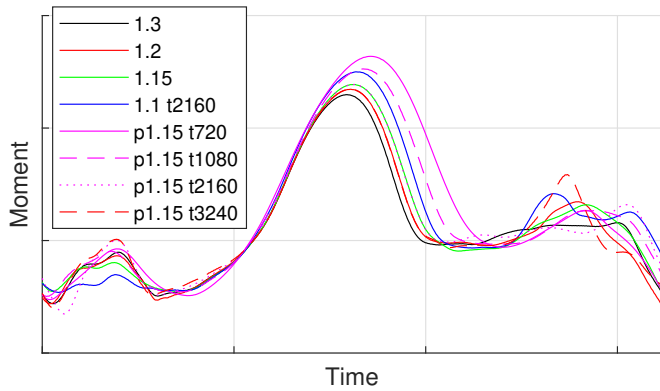
7

FIGURE 11: BOUNDARY LAYER MESH IMPACT AT FOIL SECTION 17

FIGURE 12: SELECTED PARAMETERS COMPARED TO MOST RE-FINED

The first half of the upstream stroke is very consistent, but there is significant variation in the peak. Delayed detachment of the dynamic stall vortex results in a later and larger peak torque. The general trend is that a lower expansion ratio results in later stall, and the lower the time step, the earlier the stall. Note that for the same time step and expansion ratio, the stall occurs much later for the matched outer mesh (dashed pink line compared to solid green). It appears, however, that this is driven by the larger Courant number in the matched simulation.

For the largest most refined mesh with 168.9 million cells, the peak starts to converge as the time step gets small, toward the solution found with the converged time step for the original 1.3 expansion ratio. This would indicate that the most important factor is having a time step that is converged for the particular expansion ratio.

It should be noted that all of the solutions have significant uncertainty. At the most basic level, the use of a turbulence model in all the simulations is a significant choice. The development of turbulence near the highly dynamic foil is very complex and could have real impacts on the progression of loads. In the interest of computation time, the original base combination of an expansion ratio of 1.3 with 1080 time steps per revolution was used.

Figure 12 compares the temporal and spatial distribution of the torque when using this selected combination and when using the most refined combination tested. The top right of the figure shows a time history of the net load on a single foil over two revolutions. The bottom of the figure shows the spatial torque distribution on the foil at a single instant in time; this time is marked with a dashed line in the time history, and the dashed lines in the spatial plot mark where the struts are located. The foil's position at this time is represented by the image in the upper left (flow in the positive *x*-direction). The phase offset experienced in a helical blade is evident.

There is relatively good agreement in the time history for the two mesh and time step combinations. The less refined model does experience slightly earlier stall, evident in the second quarter of the foil. In the net force, this is countered by a slightly larger force in the near-strut region.
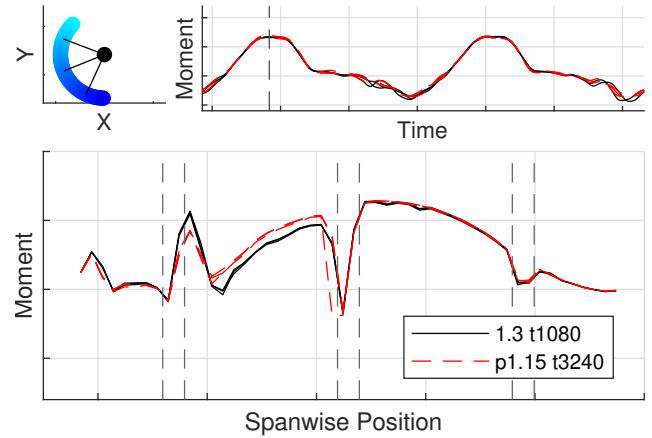
5. STRAIGHT BLADE COMPARISON

Analysis of the loads on the helical blades revealed significant three-dimensional effects. To highlight the impact of the helix, a comparison to a similar straight-bladed turbine was performed. The straight blades featured the same foil sections as the original turbine; each section along the span was rotated to the same azimuth angle to create the new geometry. This blade has the same volume and plan area as the original blade.

The base RivGen Turbine design was assessed at a full range of TSRs for load analysis. In the study of the 3D impacts of helical blades and struts, only the TSR found to produce maximum power was assessed. Both the turbine with helical blades and the turbine with straight blades were run with and without struts.

5.1 Relative Strut Influence

Figure 13 shows the moment progression through the revolution for the four configurations. The results are shown for nine characteristic foil sections along the span. The color of section number corresponds to the vertical lines in the image at the top of the figure, indicating spanwise cross sections. Blue sections are at either tip, red sections are at the struts (if the configuration includes struts), and black sections are in between, on longer segments of uninterrupted foil.

The location of the colors on the circles corresponds with the same location in the rotation, with the inflow from the left, as in the coordinate system defined in Figure 2. Again, the rotation direction is clockwise, so that the foil is moving upward on the upstream side.

It is evident how unsteady the loading is for a cross-flow turbine, and how important fatigue loading is for the structure. For all configurations, almost all the positive power production comes when the foil sections are in the middle of the upstream stroke. In all cases there is significant decline in power near the tips. This effect is symmetric in the straight blade but not for the helical blade, with a large decrease at the tip with the latest phase angle.

Table 3 shows the produced power for the four configurations, normalized with respect to the maximum, which was produced
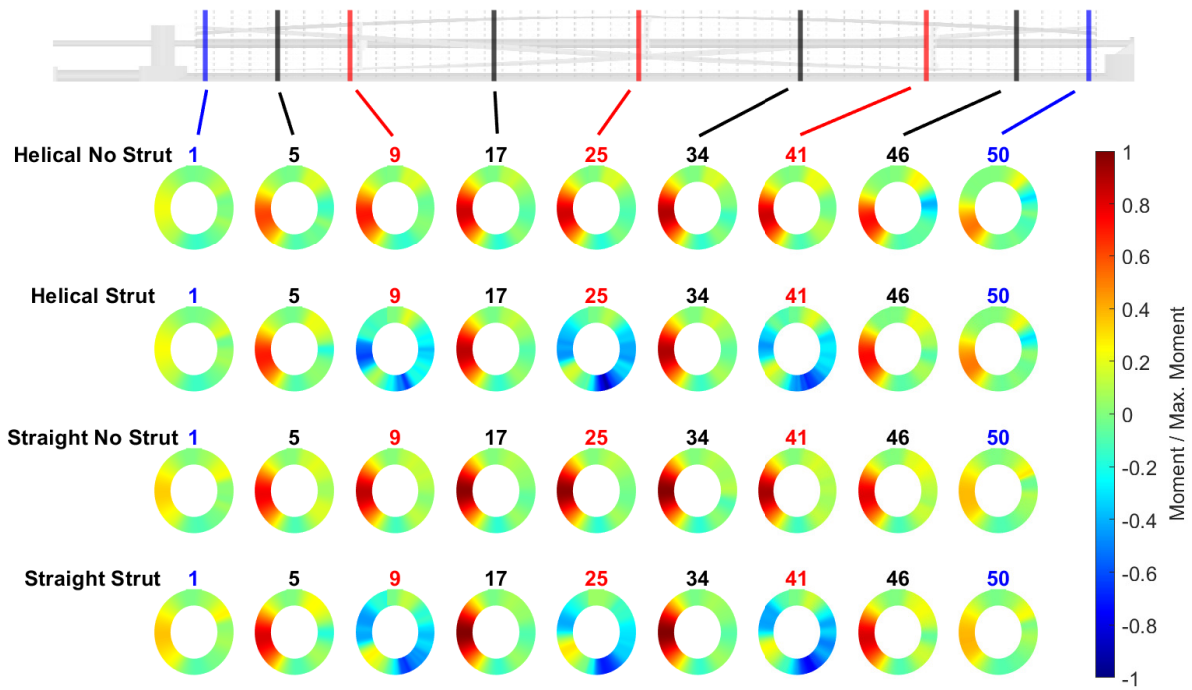
8

FIGURE 13: MOMENT THROUGH ROTATION AT CHARACTERISTIC FOIL SECTIONS (CLOCKWISE ROTATION WITH INFLOW FROM THE LEFT)

by the straight blades with no struts. The standard deviation in power is also provided. This standard deviation is relative to the mean power for the same configuration, and indicates how much fatigue loading is present.

TABLE 3: 3D INFLUENCES ON POWER

| | | Relative Net Power | |
		Mean	Standard Deviation
Straight	No Strut	100.0%	36.4%
	Strut	47.9%	72.5%
Helical	No Strut	74.4%	7.9%
	Strut	42.2%	10.2%

As expected, the straight-bladed rotor produces more net power but with much larger variations in time compared to the helical-bladed rotor. Also as expected, the presence of struts significantly reduces the produced power for both blade shapes. Since the flow is interrupted along the span by the struts, it also makes sense that the standard deviation, representing the variability in the power, increases when struts are present.

It was expected that the induced spanwise flow in the helical rotor would increase the impact of the struts, leading to relatively larger reductions in power. However, this is not the case for the RivGen Turbine. The specific blade design and helix angle experiences a smaller relative decrease in power with helical blades than straight blades. With straight blades, the power goes down by 52% when struts are introduced. With helical blades, the power only goes down by 43%.

Figure 14 and Figure 15 provide more detail on the different load paths of the four configurations. Figure 14 displays the maximum tangential and normal loads along the blade span found in a rotation. There is a slight reduction in maximum loads in both directions for the helical-bladed rotor. The three lines of each type show the forces from the three different foils during the last revolution. The slight variability between foils shows the natural uncertainty in forces on a cross-flow turbine.

Figure 15 shows the loads at the characteristic uninterrupted foil section 17. The tangential and normal force are plotted against azimuth angle, and the lift and drag coefficients are plotted against angle of attack with respect to an undisturbed inflow. These coefficient plots display the hysteresis effect that indicates dynamic stall. The rapid change in angle of attack leads to different forces at the same angle of attack in the ramp up and the ramp down. The three colors correspond to the loads on the three foils for one rotation, displaying some of the statistical cyclic variation.

6. CONCLUSIONS

A URANS CFD study was performed for the cross-flow MHK RivGen Turbine. Convergence studies were performed for the large-scale spatial discretization, the base time step, and a more detailed analysis of the boundary layer modeling. The highly dynamic loads, driven by the complex phenomenon of dynamic stall, were found to be very sensitive to these modeling parameters, pointing to the difficulty and uncertainty in cross-flow load predictions.

The cell expansion ratio in the boundary layer mesh proved to be particularly influential on the foil torque. This parameter is difficult to isolate, as a change in the expansion ratio either requires a change in the total prism layer thickness, the outer mesh size, or the abruptness of change between the prism layers
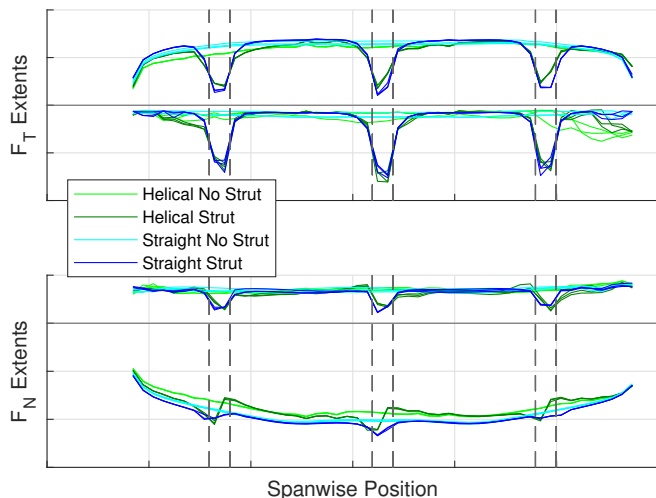
9

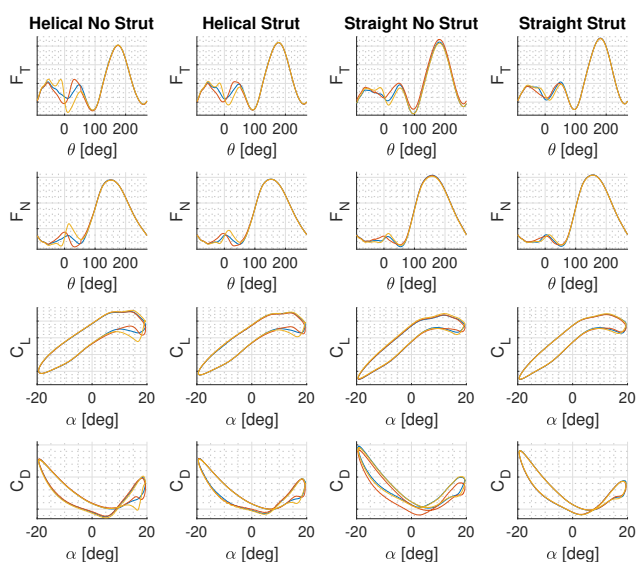**FIGURE 14: LOAD COMPARISON AT FOIL SECTION 17**

FIGURE 15: LOAD COMPARISON AT FOIL SECTION 17

and the outer mesh. The sensitivity of the time step was also found to be strongly tied to the boundary layer mesh expansion ratio.

Variations of helical and straight blades in combination with and without struts were compared, to assess the joint impact of these important 3D factors. As expected, helical blades result in a small decrease in power production, and the introduction of struts results in a large reduction in power. The results emphasize the importance of strut design, with reductions in power on the order of one-half.

For the RivGen Turbine design, the relative power loss from struts was lower when using helical foils compared to straight foils. In addition, the standard deviation of the net rotor torque compared to the average torque was more than seven times lower with helical blades. This dramatic decrease in blade fatigue loading comes at a small cost in power loss when comparing the

two blade shapes with struts.

The 3D flow effects of blade helicity and struts are very important to consider in cross-flow turbine design and have a coupled effect. CFD methods for modeling dynamic stall result in a significant amount of uncertainty, and more work needs to be done to improve predictions of this complicated flow pattern.

REFERENCES

[1] Jacobson, Cunninghan, Ravens and Scott. "Assessment and Mapping of the Riverine Hydrokinetic Resource in the Continental United States." Memorandum 1026880. Electric Power Research Institute, Palo Alto, CA. 2012.

[2] Rezaeiha, Montazeri and Blocken. "CFD analysis of dynamic stall on vertical axis wind turbines using Scale- Adaptive Simulation (SAS): Comparison against URANS and hybrid RANS/ LES." *Energy Conversion and Management* .

[3] Marsh, Penesis, Ranmuthugala and Thomas. "Numerical Investigation of the Influence of Blade Helicity on the Performance Characteristics of Vertical Axis Wind Turbines." *Renewable Energy* .

[4] Divakaran, Mohammad, Ramesh and Velamati. "Effect of Helix Angle on the Performance of Helical Vertical Axis Wind Turbine." *Energies* DOI 10.3390/en14020393.

[5] Strom, Johnson and Polagye. "Impact of Blade Mounting Structures on Cross-flow Turbine Performance." *Journal of Renewable and Sustainable Energy* DOI 10.1063/1.5025322.

[6] ORPC. "RIVGEN® Power System Integrated Microgrid Solutions." URL https://orpc.co/rivgen-power-system-integrated-microgrid-solutions/.

[7] Siemens Digital Industries Software. *Simcenter STAR-CCM+ - User Guide, version 2022.1* (2022).